

# Image Reconstruction Using a Gradient Impulse Response Model for Trajectory Prediction

S. Johanna Vannesjo,<sup>1†</sup> Nadine N. Graedel,<sup>1†</sup> Lars Kasper,<sup>1,2</sup> Simon Gross,<sup>1</sup> Julia Busch,<sup>1</sup> Maximilian Haerberlin,<sup>1</sup> Christoph Barmet,<sup>1,3</sup> and Klaas P. Pruessmann<sup>1\*</sup>

**Purpose:** Gradient imperfections remain a challenge in MRI, especially for sequences relying on long imaging readouts. This work aims to explore image reconstruction based on k-space trajectories predicted by an impulse response model of the gradient system.

**Theory and Methods:** Gradient characterization was performed twice with 3 years interval on a commercial 3 Tesla (T) system. The measured gradient impulse response functions were used to predict actual k-space trajectories for single-shot echo-planar imaging (EPI), spiral and variable-speed EPI sequences. Image reconstruction based on the predicted trajectories was performed for phantom and in vivo data. Resulting images were compared with reconstructions based on concurrent field monitoring, separate trajectory measurements, and nominal trajectories.

**Results:** Image reconstruction using model-based trajectories yielded high-quality images, comparable to using separate trajectory measurements. Compared with using nominal trajectories, it strongly reduced ghosting, blurring, and geometric distortion. Equivalent image quality was obtained with the recent characterization and that performed 3 years prior.

**Conclusion:** Model-based trajectory prediction enables high-quality image reconstruction for technically challenging sequences such as single-shot EPI and spiral imaging. It thus holds great promise for fast structural imaging and advanced neuroimaging techniques, including functional MRI, diffusion tensor imaging, and arterial spin labeling. The method can be based on a one-time system characterization as demonstrated by successful use of 3-year-old calibration data. **Magn Reson Med 76:45–58, 2016. © 2015 Wiley Periodicals, Inc.**

**Key words:** magnetic field monitoring; linear time-invariant (LTI); GIRF; single-shot imaging; EPI; spiral imaging

## INTRODUCTION

Over the past decades, gradient equipment for MRI has continually advanced to a high level of sophistication and performance. Nonetheless, present-day gradient systems still exhibit finite fidelity and remain subject to

engineering trade-offs and imperfections. These include limited coil and amplifier bandwidth, eddy current effects, mutual coupling of gradient channels, coil vibrations, thermal variation, and finite accuracy of timing calibration. The resulting deviations from nominal gradient field evolutions can be detrimental to MR techniques that pose high demands on gradient accuracy such as spiral (1) and echo-planar imaging (EPI) (2) as well as a range of more advanced strategies for covering k-space with long readout trajectories.

In EPI, residual gradient imperfections often result in ghosting artifacts and distortion whereas with spiral readouts they tend to give rise to image blurring. For spirals in particular, limited gradient fidelity has been one major obstacle to broader use. Still today, both interleaved and single-shot spiral imaging are hardly used in practice despite offering greater encoding efficiency than EPI.

Imperfections of gradient time courses have been addressed by a variety of correction strategies. For EPI, it is common to correct phase inconsistency between odd and even readout lines, using data acquired in a separate reference readout (3). Similar correction parameters can be estimated in the image domain using regions without overlaps between object and ghost (4). Alternatively, the EPI scan can be repeated with opposite polarity of the readout gradient to generate fully sampled data sets with readouts of consistent direction (5). Another class of correction methods relies on array acquisition to detect and correct for phase inconsistencies (6,7). In varying ways all of these techniques leverage the regular structure of EPI trajectories, which permits approximate correction by enforcing consistency between readout lines. Spiral trajectories are less repetitive and hence more challenging to correct. One basic correction applicable to spirals is to estimate and compensate for net delays of the individual gradient chains (8), an approach that has recently been expanded to k-space position-dependent delays (9).

The effectiveness of these correction methods depends on the validity of the underlying explicit or implicit model assumptions. For instance, enforcing consistency between odd and even readout lines in EPI will only be adequate when field imperfections are the same for all odd and even legs, respectively. This assumption will be violated for example in the presence of eddy currents or mechanical oscillations whose net effect will vary with gradient pulse history. Assuming global gradient delays is an even stronger simplification, which is rendered inadequate by any mechanism that makes the net system response frequency-dependent, including eddy currents, mechanical resonances, and the general low-pass behavior of gradient coils and amplifiers. Addressing these

<sup>1</sup>Institute for Biomedical Engineering, University of Zurich and ETH Zurich, Zurich, Switzerland.

<sup>2</sup>Translational Neuromodeling Unit, Institute for Biomedical Engineering, University of Zurich and ETH Zurich, Zurich, Switzerland.

<sup>3</sup>Skope Magnetic Resonance Technologies, Zurich, Switzerland

Grant sponsor: Swiss Commission for Technology and Innovation; Grant number: KTI 13756.1 PFFLM-NM.

<sup>†</sup>Present address: FMRIB centre, Nuffield Department of Clinical Neurosciences, University of Oxford, Oxford, UK.

\*Correspondence to: Klaas P. Pruessmann, Ph.D., Institute for Biomedical Engineering, University and ETH Zurich, Gloriastrasse 35, CH-8092 Zurich, Switzerland. E-mail: pruessmann@biomed.ee.ethz.ch

Received 18 March 2015; revised 19 June 2015; accepted 20 June 2015

DOI 10.1002/mrm.25841

Published online 27 July 2015 in Wiley Online Library (wileyonlinelibrary.com).

© 2015 Wiley Periodicals, Inc.

effects requires a more general correction approach without assumptions regarding the nature of field imperfections or the trajectory shape.

An established method that does not rely on mechanistic models of field imperfections is to measure actual k-space trajectories and use them as the basis of image reconstruction (10–12). Several techniques exist for trajectory measurement. Some are based on MR acquisitions from a phantom or directly from the subject (12–14). These, however, generally require slight modification of the imaging sequence and rely on repeated acquisition for each gradient direction. A faster alternative is to use a dynamic field camera based on NMR field probes (15–18), which permits recording the full spatiotemporal field evolution in a single acquisition and without sequence modification. Similar to phantom-based trajectory mapping, field-camera measurements can be carried out separately, before or after actual scanning. However, all approaches that rely on separate trajectory measurements require significant additional scan time, since trajectories generally need to be measured for every specific combination of sequence parameters and geometry of the imaging volume. A more efficient alternative is to perform field-camera measurements concurrently with actual imaging, using non-proton field probes, typically based on  $^{19}\text{F}$  NMR (19–22). This however requires simultaneous heteronuclear receive capability and adds to the complexity of data acquisition and signal processing. Moreover, both concurrent monitoring and separate field camera trajectory measurements come with substantial additional hardware requirements.

A less hardware-intensive solution is to depart from measuring individual k-space trajectories and instead aim to characterize the behavior of the gradient system comprehensively in a one-time effort. Such characterization is greatly simplified by modeling the gradient system as linear and time-invariant (LTI). Under this assumption its behavior is fully described by its impulse response functions. The gradient impulse response functions (GIRF) can be determined by measuring field responses to known input waveforms (23–25). Based on known GIRFs, actual field dynamics can readily be predicted from given demand waveforms for any type of sequence.

The aim of the present work is to explore the utility of broadband GIRF characterization for image reconstruction. To challenge the concept, we focus on single-shot EPI and spiral trajectories with long acquisition windows. The performance of GIRF-based image reconstruction is studied in a phantom and in vivo on a commercial 3 Tesla (T) system. The results are assessed by comparison with reconstructions based on concurrent field monitoring, separate trajectory measurements, and nominal trajectories.

## METHODS

### GIRF-based Trajectory Prediction

Gradient system characterization as described in Vannesjo et al (24) was performed on a 3T Philips Achieva whole-body system (Philips Healthcare, Best, The Netherlands), with the manufacturer’s built-in eddy current compensation activated. In brief, 12 different triangular pulses (slew rate 180 T/m/s, time-to-peak 50–160  $\mu\text{s}$  at 10- $\mu\text{s}$  incre-

ments, 50 repetitions) were given as input to each gradient channel separately. The resulting field responses were measured with a dynamic field camera consisting of 16  $^1\text{H}$  NMR field probes distributed on the surface of a sphere of 10 cm radius (15–18). Spherical harmonic basis functions up to 1<sup>st</sup> order were fitted to the probe measurements, yielding linear gradient field terms in the three orthogonal directions, as well as a 0<sup>th</sup>-order field term, reflecting global field shifts. Each field term was treated as an output channel of a multiple-input, multiple-output LTI system. The GIRFs were calculated by frequency-domain division of the measured output,  $O^{(meas)}(\omega)$ , by the known inputs,  $I(\omega)$ , using least-squares combination of data from different input pulses (24):

$$GIRF_{l,m}(\omega) = \frac{\sum_j I_{l,j}^*(\omega) \cdot O_{l,m,j}^{(meas)}(\omega)}{\sum_j |I_{l,j}(\omega)|^2}, \quad \begin{array}{l} l = x, y, z \\ m = 0, x, y, z \\ j = 1, 2, 3 \dots \end{array} \quad [1]$$

where  $l$ ,  $m$ , and  $j$  denote the input gradient channel, output field term and input pulse, respectively, and  $*$  denotes the complex conjugate.

Before the current study, GIRFs had already been measured on the same MR system using identical methods. Hence, two sets of measured GIRFs were available for use, obtained with an interval of 3 years. Where relevant, the previously measured GIRFs will be termed “GIRF, 3 years prior”. Self-term (i.e.,  $l = m$ ) GIRFs from both measurement occasions are shown in Figure 1 (time domain) and Figure 2 (frequency domain).

GIRF-based prediction of gradient output,  $O^{(pred)}(\omega)$ , in response to given input gradient waveforms was performed by frequency-domain multiplication of the input with the measured GIRFs:

$$O_m^{(pred)}(\omega) = \sum_l I_l(\omega) \cdot GIRF_{l,m}(\omega). \quad [2]$$

For discrete implementation of this operation, the input waveforms were bilaterally zero-padded in the time domain such as to match the maximum temporal extent of the system response. Discrete Fourier transform (DFT) was then used to calculate the corresponding discrete versions of  $I_l(\omega)$ . In the frequency domain, the given GIRFs were regridded to match the sampling pattern of the discrete input spectra, followed by per-frequency multiplication and summation. From the resulting output spectrum, the discrete form of  $o^{(pred)}(t)$  was then obtained by inverse DFT. The time integral of  $o^{(pred)}(t)$  yielded the set of phase coefficients:

$$k_m^{(pred)}(t) = \gamma \int_0^t o_m^{(pred)}(\tau) d\tau. \quad [3]$$

For comparison, the nominal k-space coefficients,  $k^{(nomi)}(t)$ , were similarly obtained by taking the time-integral of the input gradient waveforms,  $i(t)$ :

$$k_l^{(nomi)}(t) = \gamma \int_0^t i_l(\tau) d\tau. \quad [4]$$

As apparent from the equations above, the GIRF-based predictions included both cross-term responses between

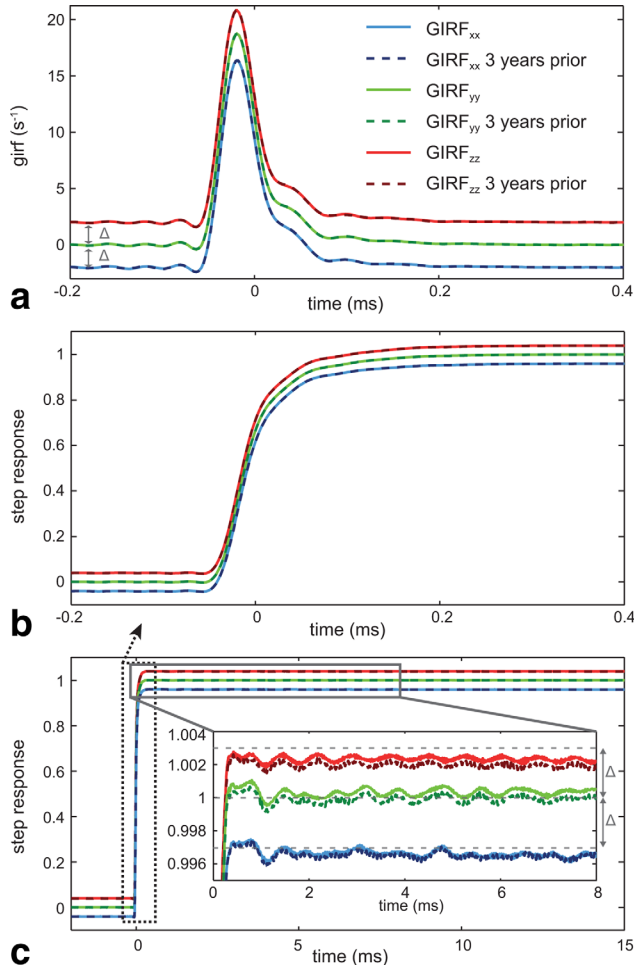


FIG. 1. Measured self-term GIRFs in the time domain for recently acquired and 3-year-old GIRFs, showing impulse responses (a) and step responses (b,c). For display purposes, the curves of the three different gradient axes have been offset to each other by a constant,  $\Delta$ .

1<sup>st</sup>-order field terms and 0<sup>th</sup>-order field responses generated by gradient operation. Nominal k-space trajectories per definition assume self-term output only.

### Field Monitoring

Each imaging gradient sequence was, furthermore, measured in a separate scan, here termed “premonitoring,” using a dynamic field camera with 16 <sup>1</sup>H field probes. The premonitoring served to capture reproducible field perturbations, including potential nonlinear system responses that are not included in the LTI model. Additionally, concurrent field monitoring (25) with 16 <sup>19</sup>F field probes was used during all imaging acquisitions. Concurrent monitoring reflects the actual fields present upon image encoding, including potential deviations from reproducible system responses. To evaluate the performance of the GIRF approach as well as its limitations, concurrently monitored trajectories were, therefore, used as a reference for comparisons. For both concurrent monitoring and premonitoring, spherical harmonic basis functions of 0<sup>th</sup>–1<sup>st</sup> order were fitted to the measured probe phases, yielding a set of measured phase coefficients,

$k^{(meas)}(t)$ . Temporal differentiation of  $k^{(meas)}(t)$  yielded the measured fields,  $o^{(meas)}(t)$ , of 0<sup>th</sup> and 1<sup>st</sup> order:

$$o_m^{(meas)}(t) = \frac{1}{\gamma} \cdot \frac{dk_m^{(meas)}(t)}{dt} \quad [5]$$

### Concomitant Field Correction

One known cause for deviation from the linearity assumption of the LTI system model is gradient-induced concomitant fields. To a first approximation, the concomitant fields amount to a set of second-order field terms, which scale with the square of the gradient strength (26). These field terms are not spanned by the spherical-harmonic basis used for field monitoring and thus cause errors in the field expansions. To remove such errors, concomitant field correction for all field monitoring was performed as follows. Initially, measured gradient time-courses were determined from uncorrected probe data, as described above. In the next step, the induced concomitant fields were calculated based on the measured gradients, using an analytical model for the concomitant field terms:

$$B_C(x, y, z, t) = \frac{1}{2B_0} \left\{ \left[ G_x^2(t) + G_y^2(t) \right] z^2 + G_z^2(t) \frac{x^2 + y^2}{4} - G_x^2(t) G_z^2(t) xz - G_y^2(t) G_z^2(t) yz \right\}. \quad [6]$$

Subsequently, the phase induced by concomitant fields at the position of each field probe was calculated and subtracted from the measured phase evolutions. In the final step, the thus corrected probe phase evolutions were used to repeat the 0<sup>th</sup>- and 1<sup>st</sup>-order spherical harmonic fitting. The correction predominantly affected the 0<sup>th</sup>-order field term, as the 1<sup>st</sup>-order fields are orthogonal to the concomitant field terms. It was observed that an apparent time-linear component in the measured 0<sup>th</sup>-order phase coefficients of EPI and spiral gradient sequences was indeed removed by the correction.

### Data Acquisition

Image data of a spherical water-filled phantom and a healthy volunteer was acquired with an eight-channel receive head coil (Philips Healthcare, Best, Netherlands). Written informed consent was obtained from the volunteer before scanning, in compliance with local ethics guidelines.

Single-shot k-space sampling trajectories of three different types were used: EPI, spiral, and variable-speed EPI, (VS-EPI) (Figs. 3a–i). Corresponding gradient sequences were calculated using 31 mT/m maximum gradient amplitude and 200 mT/(m·ms) slew rate. For the spirals, the time-optimal gradient sequence yielding the desired k-space coverage was obtained as described in Lustig et al (27). The variable-speed EPI was designed as described in Kasper et al (28), matching acquisition weighting to Gaussian image smoothing for fMRI applications.

The spectral profiles of the gradient sequences depend both on the class of trajectory and on the imaging parameters, particularly the image resolution. To cover different frequency compositions, images with different in-

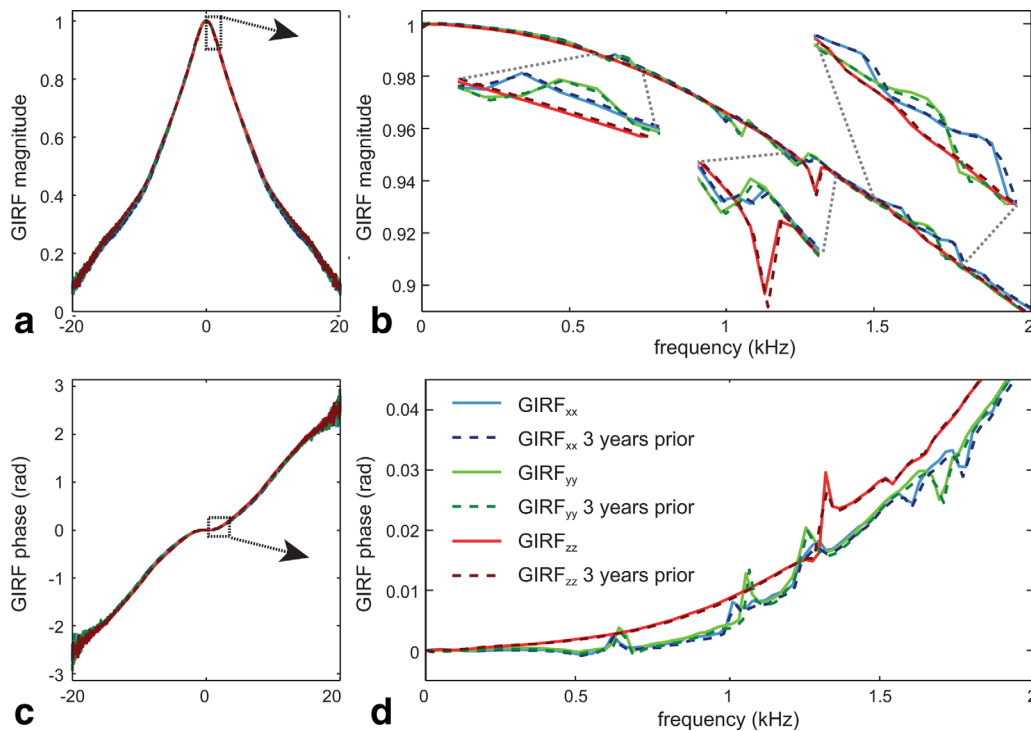


FIG. 2. Measured self-term GIRFs in the frequency domain for recently acquired and 3-year-old GIRFs, showing magnitude (a,b) and phase (c,d) responses.

plane resolution were acquired for the normal EPI (1.75–3.00 mm) and spiral trajectory (1.35–2.00 mm in-plane) (Figs. 3j–o). Furthermore, for a representative selection of commonly used single-shot imaging techniques, acquisition acceleration by parallel imaging was used for the higher resolutions, using the SENSE approach (29). High-resolution EPIs and spirals were acquired with an undersampling factor of 2 and the VS-EPI was acquired with a nominal resolution of 1.80 mm and undersampling factor of 3. For each sequence, five slices were obtained with  $\text{FOV} = 23 \times 23 \text{ cm}^2$ , slice thickness = 3 mm and volume  $\text{TR} = 3 \text{ s}$ . Readout length ( $T_{\text{RO}}$ ) and TE varied with trajectory, and the latter was kept as short as possible for the phantom data. Phantom images were acquired in all three orthogonal slice directions for a subset of the used trajectories, and in transverse orientation for all trajectories. In vivo, angulated transverse slices of the brain were acquired and TE was adjusted to yield  $T_2^*$ -weighted image contrast. A summary of all acquisition parameters is given in Table 1.

For correction of static  $B_0$  nonuniformity, field maps were acquired with the same slice geometry as the single-shot images. The field maps were based on two spin-warp GRE images with different TE ( $\text{FOV} = 23 \text{ cm}$ , resolution = 3 mm isotropic,  $\text{TE}_1/\text{TE}_2 = 2.0/4.3 \text{ ms}$ ,  $\text{TR} = 1.6 \text{ s}$ ), from which the phase difference divided by the echo time difference yielded the static frequency offsets. The acquisition with shorter TE also served as the coil sensitivity reference for SENSE reconstruction.

### Image Reconstruction

Image reconstruction was performed with the iterative approach described in Pruessmann et al (29), including forward and reverse gridding (30–32), sensitivity encod-

ing where applicable, and multifrequency interpolation for  $B_0$  correction (33–35). For fully sampled trajectories, per-coil reconstructions were merged by root-sum-of-squares combination.

Each dataset was reconstructed using nominal, predicted, premonitored, and concurrently monitored trajectories. Predicted trajectories were obtained using both the old and the recently measured GIRFs. To elucidate the utility of mere delay correction, reconstructions based on nominal trajectories were performed with and without time shift by the apparent delay. The apparent delay was determined such as to minimize the mean-square deviation between the delayed nominal and concurrently monitored trajectories.

To account for spatially uniform phase modulations, imaging data was demodulated by the measured or predicted 0<sup>th</sup>-order phase coefficient,  $k_0(t)$ , before reconstruction. For the nominal trajectories,  $k_0(t)$  was assumed to be zero throughout. Reconstruction based on GIRF-predicted trajectories was performed both with and without demodulation to investigate the significance of 0<sup>th</sup>-order cross-term predictions.

In some of the concurrently monitored  $k_0(t)$ , a time-linear component stemming from slow 0<sup>th</sup>-order field drift was present. A time-linear spatially uniform phase induces a shift in the image for EPI sampling schemes and blurring in spiral acquisitions. A slow field drift is relatively straightforward to measure and counteract with navigators, not requiring additional hardware or special sequences. Therefore, for better comparison between nominal, predicted and concurrently monitored reconstructions, this linear component was added to  $k_0^{(\text{nomi})}(t)$ ,  $k_0^{(\text{pred})}(t)$  and premonitored  $k_0$  before image reconstruction.

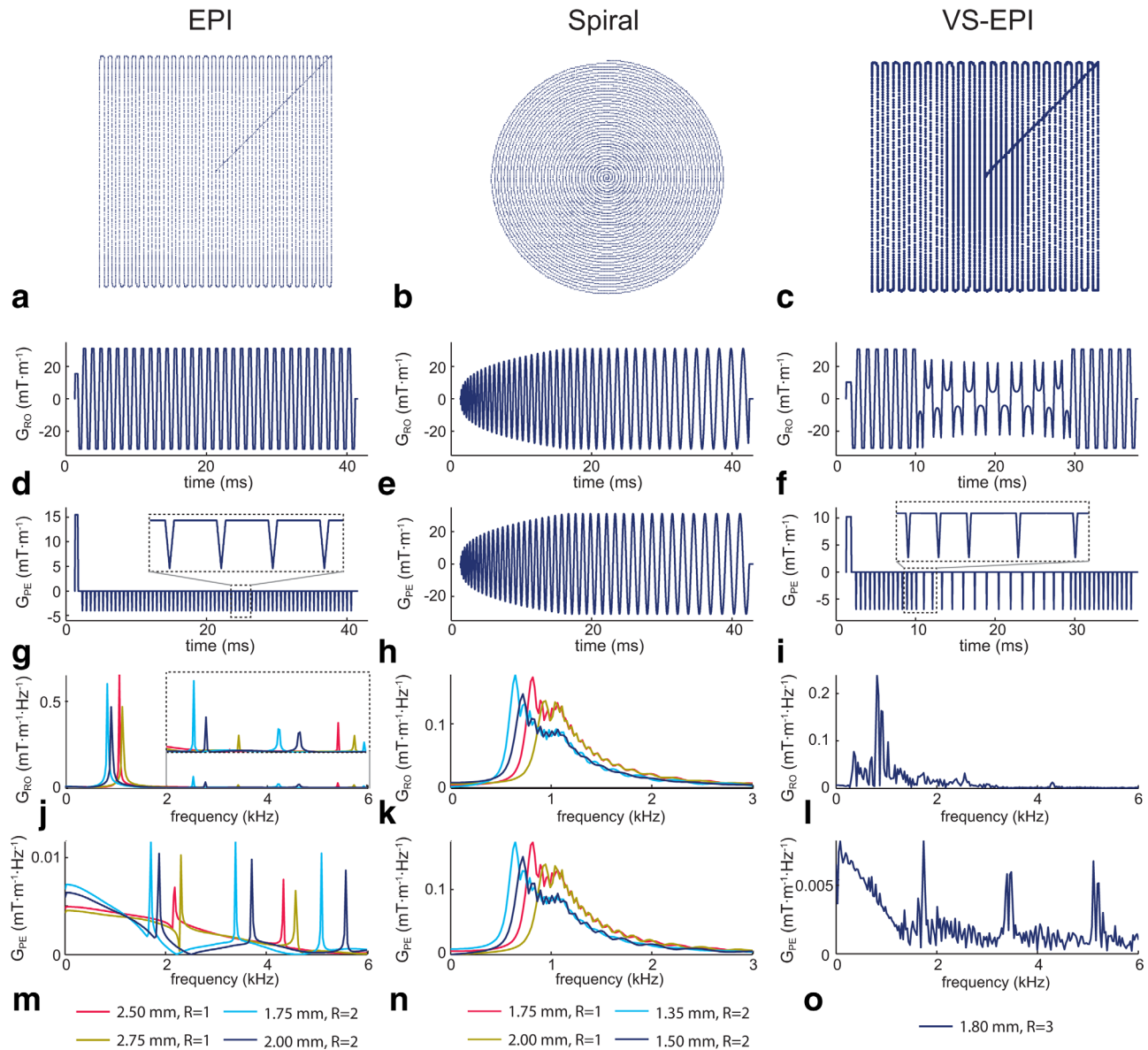


FIG. 3. Input EPI, spiral, and VS-EPI sequences. Time-domain plots show one representative EPI/spiral sequence each, whereas frequency-domain plots show all acquired sequences. **a-c**: Nominal k-space sampling trajectories. **d-f**: Input readout gradient ( $G_{RO}$ ). **g-i**: Input phase-encoding gradient ( $G_{PE}$ ). **j-l**: Spectra of input readout gradients. **m-o**: Spectra of input phase-encoding gradients.

In summary, each dataset was reconstructed using the following k-space trajectories: (a) Nominal; (b) Nominal, delay-corrected; (c) GIRF-predicted, no 0<sup>th</sup>-order phase demodulation; (d) GIRF-predicted using GIRF from 3 years prior, incl. 0<sup>th</sup>-order phase demodulation; (e) GIRF-predicted, including 0<sup>th</sup>-order phase demodulation; (f) Premonitored; (g) concurrently monitored.

## RESULTS

The measured GIRFs showed excellent stability over a time interval of 3 years, as demonstrated in Figure 1 (time domain) and Figure 2 (frequency domain). The overall shape of the system responses, as well as the center frequency, amplitude and width of specific resonances were well preserved. Root-mean-square (RMS) magnitude differences between the GIRFs acquired

recently and 3 years prior are shown in Supporting Table S1, which is available online, for self- and cross-terms, evaluated within different frequency bands. Due to increased noise in the measured GIRFs at higher frequencies (24), the RMS difference also increases with frequency. The cross-terms tended to have lower RMS difference than the self-terms, except in the lowest frequency band. For all GIRFs, the RMS difference was below 0.1% up to 10 kHz and maximally 1% at higher frequencies.

Figure 4a shows zoomed details of nominal, concurrently monitored and GIRF-predicted trajectories for representative EPI, spiral, and VS-EPI acquisitions. The monitoring results deviate significantly from the nominal trajectories in all cases. For the EPI trajectories, the largest deviation is observed at the turns of the trajectory, where the maximum actual k-value reached in the

Table 1  
Imaging Parameters of the Acquired Single-Shot Sequences

	Trajectory	Orientation	FOV (mm)	Slice (mm)	SENSE	Res (mm)	TE (ms)	T <sub>RO</sub> (ms)	TR (ms)
<i>phantom</i>	EPI	tra	228	3	1x	2.50	23	43	3000
		tra/cor/sag	228	3	1x	2.75	20	37	3000
		tra/cor/sag	228	3	2x	1.75	21	40	3000
		tra	228	3	2x	2.00	17	32	3000
	Spiral	tra/cor/sag	228	3	1x	1.75	1.4	52	3000
		tra	228	3	1x	2.00	1.4	42	3000
		tra/cor/sag	228	3	2x	1.35	1.4	41	3000
		tra	228	3	2x	1.50	1.4	34	3000
	VS-EPI	tra/cor/sag	228	3	3x	1.80	21	36	3000
	<i>in vivo</i>	EPI	angulated transversal	228	3	1x	3.00	28	32
			228	3	2x	1.75	28	40	3000
Spiral			228	3	1x	1.75	21	52	3000
			228	3	2x	1.35	21	41	3000
VS-EPI			228	3	3x	1.80	28	36	3000

readout direction is slightly less than prescribed, corresponding to a slight reduction of effective resolution. This compression is expected due to the low-pass characteristics of the gradient system, and will vary with the main frequency of the EPI readout gradient. In the spiral case, the nominal and measured trajectories gradually separate at the center to subsequently keep an approximately constant difference of approximately one Nyquist  $\Delta k$  for the rest of the readout. Similarly to the EPI, this also leads to a slightly lower  $k_{\max}$  than prescribed. The GIRF-predicted trajectories closely follow the measured ones for all three classes of trajectories. The RMS difference between nominal and concurrently monitored trajectories for the EPI, spiral and VS-EPI shown in Figure 4a was 35.9, 42.8, and 24.5 rad/m, respectively. Over all trajectories, the RMS difference was in the range of 24.5–44.3 rad/m. For GIRF-predicted versus concurrently monitored trajectories, the corresponding range was 1.5–10.2 rad/m, and the RMS difference in the three trajectories displayed in Figure 4a was 3.0, 9.2, and 1.5 rad/m for the EPI, spiral and VS-EPI, respectively.

Figures 4b and 4c show the corresponding gradient and k-coefficient time courses in the readout direction for nominal, delay-corrected nominal, GIRF-predicted, and concurrently monitored data. Differences to concurrently monitored gradients/trajectories are displayed in the lower plots. In the gradient time courses, the low-pass characteristics of the gradient system cause smoothing of sharp turns and reduced peak values. Deviations between the nominal and the measured gradients reach 3 mT/m, whereas for the GIRF-predicted versus the measured gradients it is less than 0.1 mT/m. In the k-coefficients ( $k_{RO}$ ), the largest deviations for the EPIs are again observed at the turning points. The deviation between the nominal and the measured  $k_{RO}$  in these locations is around 48 rad/m, corresponding to almost two  $\Delta k$ , as compared to 1 rad/m difference between the GIRF-predicted and the measured  $k_{RO}$ . Delay correction of the nominal trajectory has a significant impact on the trajectory in the fully sampled standard EPI case only.

Figure 4d shows the concurrently monitored and GIRF-predicted  $k_o(t)$ . The measured 0<sup>th</sup>-order phase oscillates considerably at the EPI/spiral readout frequency,

with peak-to-peak amplitudes of approximately 0.6 rad. This feature is largely predicted by the GIRF for all trajectory types. Apart from the oscillations, which are closely coupled to the readout gradient, a slower trend can be observed in the measured  $k_o$ . This slow trend is not captured by the GIRF prediction, indicating that it is most likely not linearly related to the input waveforms.

Figure 5 shows transverse magnitude images of the phantom for all reconstruction types as listed in the Methods section. In the bottom row of each sub-figure, the differences to the corresponding reconstructions based on concurrent monitoring are displayed. The difference images are scaled to percent of the maximum value in the latter.

All EPI reconstructions based on nominal trajectories showed strong ghosting artifacts (Figs. 5a,c,e). With delay correction, the ghosts were reduced in the fully sampled EPI (Fig. 5a), but not in the undersampled or variable-speed EPI (Fig 5c,e). In comparison, reconstructions based on concurrently measured trajectories had only minimal ghost levels that were not visible in linear-scale images, except for a subtle ghost in the VS-EPI. Using premonitored instead of concurrently measured trajectories slightly increased artifact levels, but still yielded very good image quality. Notably, images reconstructed based on GIRF-predicted trajectories were of similar quality as using premonitored trajectories and only slightly inferior to concurrent monitoring. Furthermore, no difference in image quality was observed between using the recently measured GIRFs and using the GIRFs from 3 years prior. However, leaving out the predicted  $k_o(t)$  in the reconstruction resulted in substantial image degradation in the standard EPI cases. Besides ghosting, geometric distortion in the form of compression in the readout direction was observed in reconstructions based on nominal trajectories for all EPI sequences. This compression corresponds to the compression of the actual trajectory in the readout direction observed in Figure 4a. The geometric congruency between images based on concurrently monitored, premonitored and GIRF-predicted trajectories was very good, with only minor differences observable at the edges of the phantom.

In the spiral images, severe blurring was observed in the nominal reconstructions, which was not improved

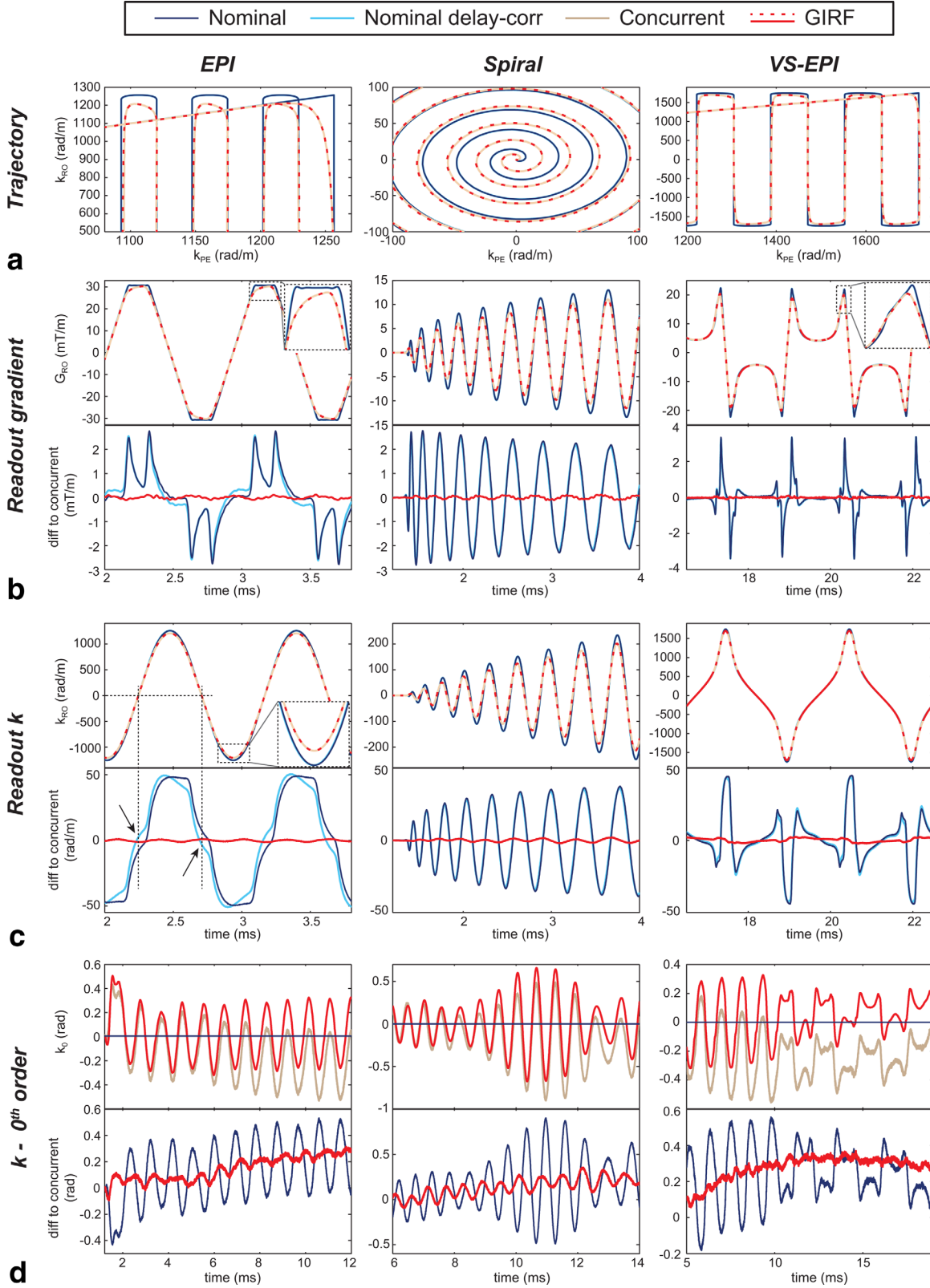


FIG. 4. Comparison of nominal, nominal delay-corrected, GIRF-predicted and concurrently monitored trajectories (a), readout gradients ( $G_{RO}$ ) (b), readout k-coefficients ( $k_{RO}$ ) (c), and  $k_0$  (d) for a representative EPI, spiral and VS-EPI acquisition. Lower plots in (b–d) show differences to concurrent monitoring.

by delay correction. The reconstructions based on concurrent monitoring showed sharply delineated images. Premonitored trajectories yielded similarly sharp

images, with minimal differences at the borders only. As judged by the difference images, artifacts were slightly increased in the GIRF-reconstructed images,

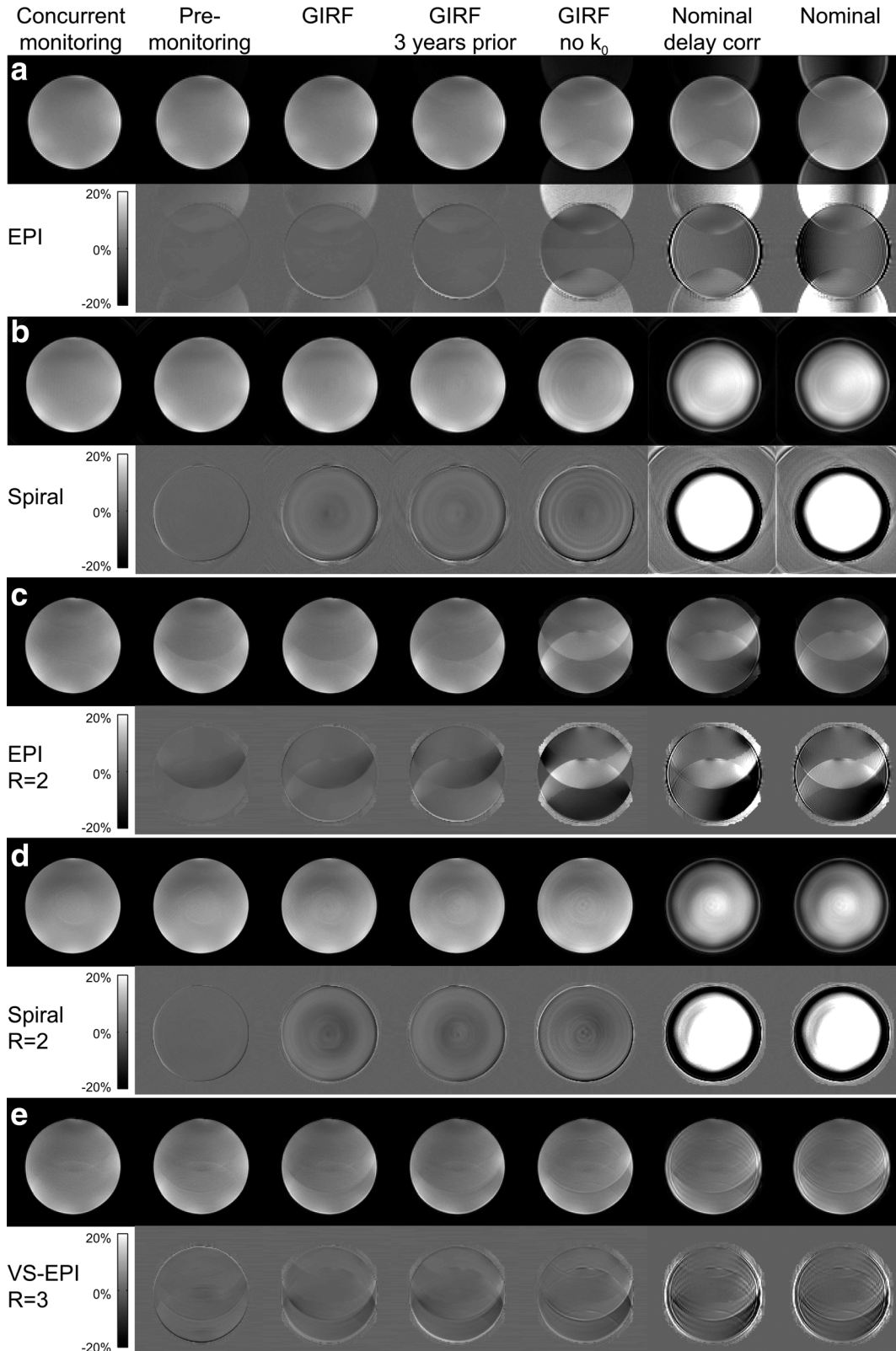


FIG. 5. Phantom images of selected EPI (a,c), spiral (b,d), and VS-EPI (e) trajectories in the transverse slice orientation. All of the performed reconstruction types are shown, as well as difference images using the reconstruction with concurrently monitored trajectories as a reference. Difference images are scaled to  $\pm 20\%$  of maximum image value in the concurrently monitored image.

especially at the center and borders of the phantom. However, GIRF-based reconstruction still yielded highly superior image quality compared with the nomi-

nal case or mere delay correction. Not using the predicted  $k_0(t)$  in the reconstruction again increased artifacts visibly.

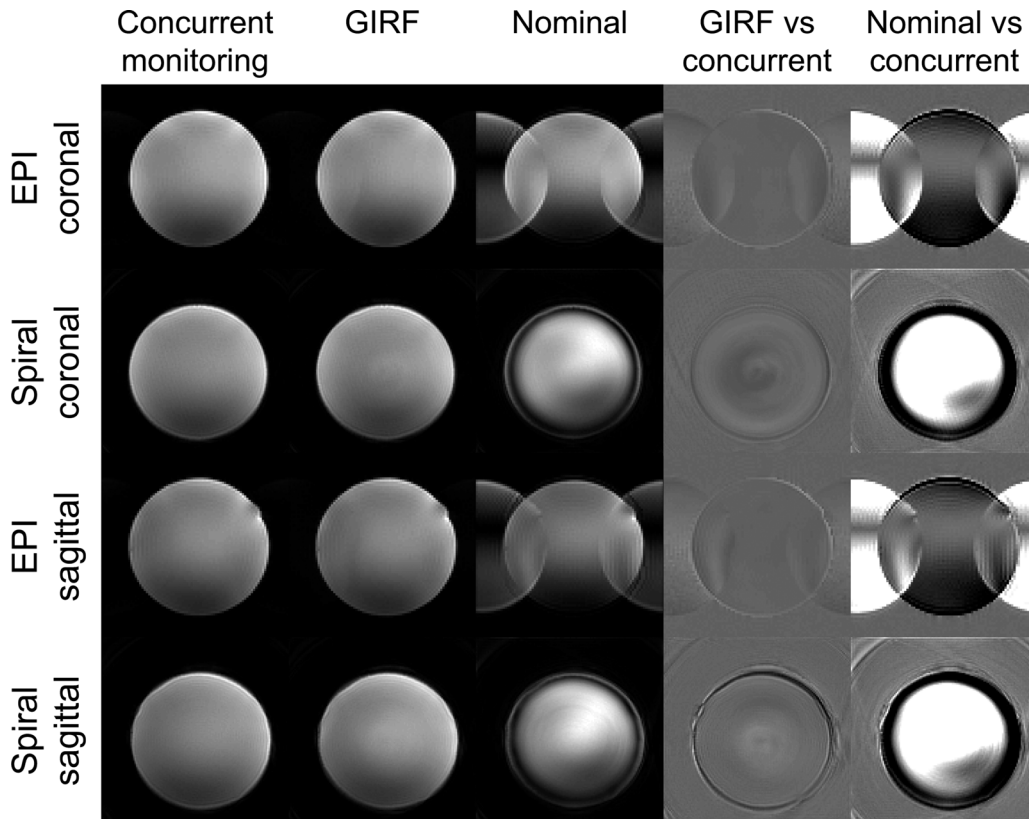


FIG. 6. Coronal and sagittal phantom images for fully sampled EPI and spiral acquisitions. Reconstructions based on concurrent monitoring, GIRF-predicted trajectories and nominal trajectories are shown, as well as difference images using the reconstruction with concurrently monitored trajectories as a reference. Difference images are scaled to  $\pm 20\%$  of maximum image value in the concurrently monitored image (gray scale as given in Figure 5).

Phantom images acquired in the coronal and sagittal slice direction are shown in Figure 6. Similarly as for the transverse images, the reconstructions based on nominal trajectories show strong artifacts, whereas the reconstructions based on concurrent monitoring or GIRF-prediction yield good and comparable image quality, with minimal differences only. Difference images are scaled as in Figure 5.

Using concurrent monitoring as a reference, the image differences for all phantom acquisitions and reconstructions are quantified in Figure 7. The values shown are the root-mean-square of the differences in image magnitude over all voxels, scaled to percent of the maximum image value in the reconstruction based on concurrent monitoring. Nominal reconstructions show large differences in all cases, especially for spiral imaging. It is interesting to note that delay correction does not always reduce image differences. Significant improvement due to delay correction is only observed for the fully sampled EPI trajectories. In almost all cases, the closest match of concurrent monitoring was accomplished with premonitoring. However, GIRF-prediction came very close throughout, with no systematic difference between using the recently measured GIRFs or the GIRFs from 3 years prior. Not including the predicted  $k_0$  in the reconstruction yielded considerably higher differences for the transverse images, especially for standard EPI trajectories. In the other slice directions, no systematic differ-

ences to GIRF-predicted reconstructions including  $k_0$  are observed.

In vivo results are shown in Figures 8 and 9, for EPI and spiral trajectories, respectively. As for phantom images, nominally reconstructed EPI images show strong ghosting and geometric distortions, whereas spiral images are severely blurred. Similar to the phantom study, concurrent monitoring enabled high-fidelity image reconstruction that was practically matched by GIRF prediction. Notably, images without apparent ghosting or blurring were also obtained with SENSE acceleration, which generally increases sensitivity to any errors in the signal model underlying image reconstruction. Static  $B_0$  correction was crucial particularly in reconstructing the spiral data. Nonetheless the unaccelerated spiral images illustrate that  $B_0$  correction alone can reach its limits in regions of excessive net phase distortion as found at the surface of the brain. This problem was addressed effectively by the boost in radial pixel bandwidth afforded by SENSE acceleration, yielding superior single-shot spiral imaging at an in-plane resolution of 1.35 mm. Variable-speed EPI, finally, proved equally amenable to GIRF-based reconstruction.

## DISCUSSION AND CONCLUSION

The results presented above demonstrate that GIRF-based trajectory prediction enables high-quality image reconstruction for technically challenging long single-

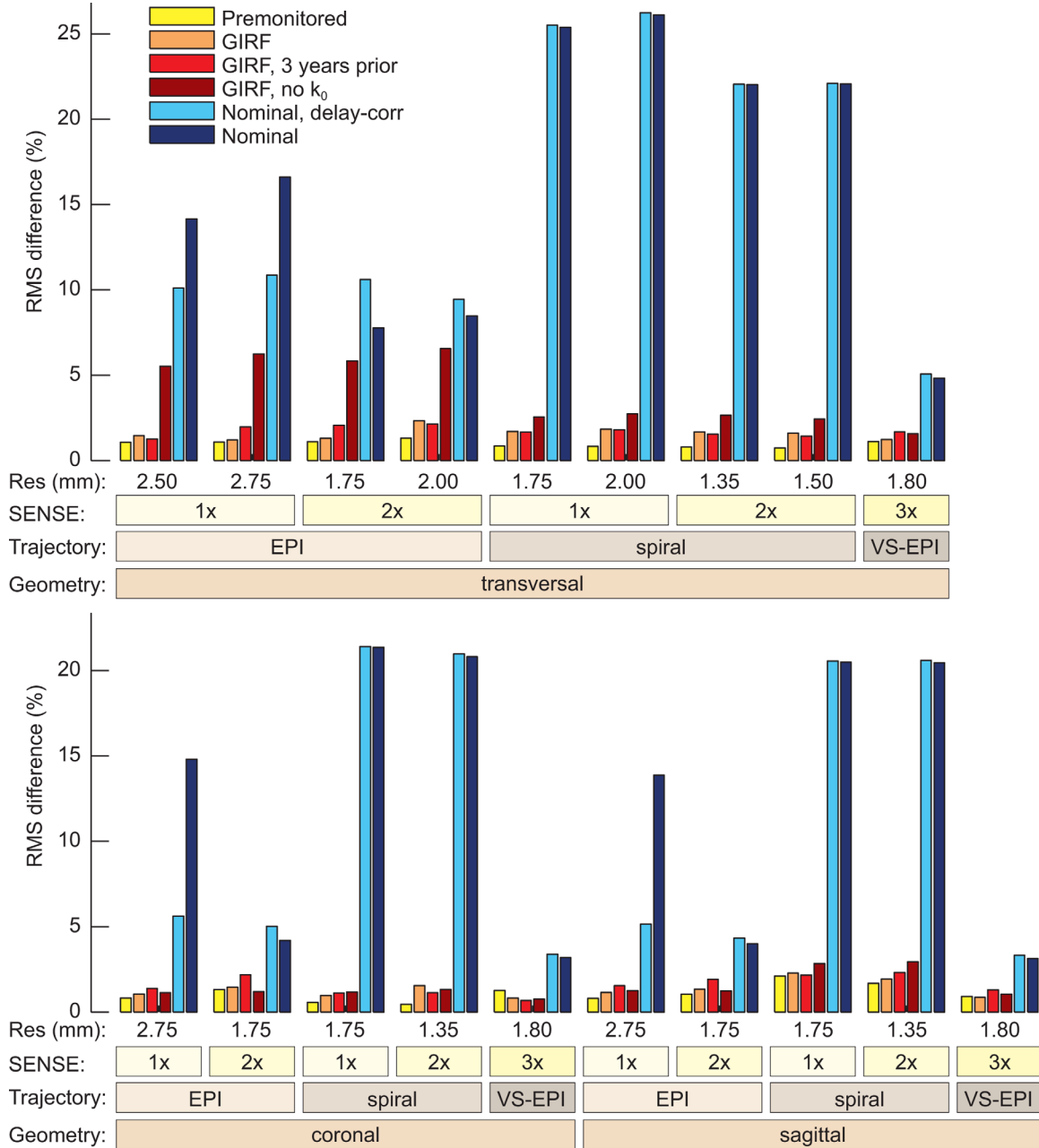


FIG. 7. Quantification of difference images for all phantom reconstructions, using the concurrently monitored reconstruction as a reference in each case. The numbers represent the root-mean-square difference over all voxels, scaled to percent of the maximum image value in the concurrently monitored image.

shot readouts of various shapes. The GIRF-based method is not restricted to any particular type of trajectory, and thus has the potential to work as a generic correction method for reproducible gradient imperfections. It could thus potentially eliminate the need for application-dependent correction techniques, which often require acquisition of reference or calibration data, added scan time, or sequence alterations. GIRF-based trajectory calculation offers this capability with substantially less hardware implications than concurrent field monitoring, by relying solely on a one-time system characterization. In this work, system stability over a time-scale of years has been observed, indicating that the one-time calibra-

tion approach may indeed be feasible on current MRI platforms.

In particular, the GIRF approach has delivered high-resolution single-shot spiral imaging of excellent quality. Spiral sampling holds several theoretical advantages over EPI, but has hitherto been notoriously difficult to perform in practice. The results of this work suggest that GIRF-based trajectory prediction in concert with algebraic  $B_0$  correction may facilitate the eventual broader deployment of single-shot spiral readouts, particularly for neuroimaging applications such as fMRI, DTI, and ASL.

Non-Cartesian imaging in general is highly susceptible to the effects of gradient imperfections. In recent years,

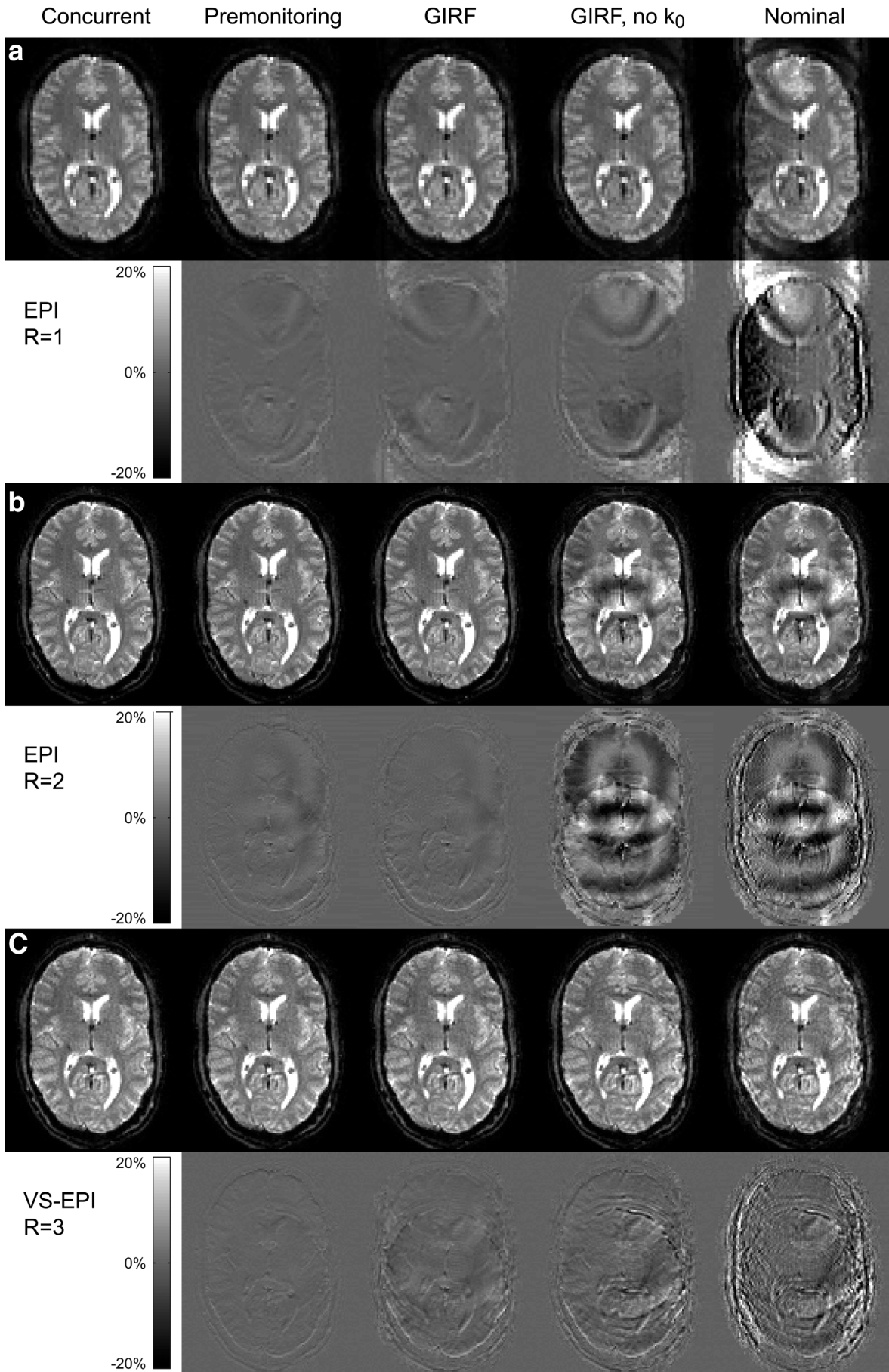


FIG. 8. **a–c**: In vivo images of the acquired EPI and VS-EPI trajectories. Reconstructions based on concurrent monitoring, premonitoring, GIRF-predicted trajectories, GIRF-predicted trajectories excluding  $k_0$ , and nominal trajectories are shown, as well as difference images using the reconstruction with concurrently monitored trajectories as a reference. Difference images are scaled to  $\pm 20\%$  of the maximum image value in the concurrently monitored image.

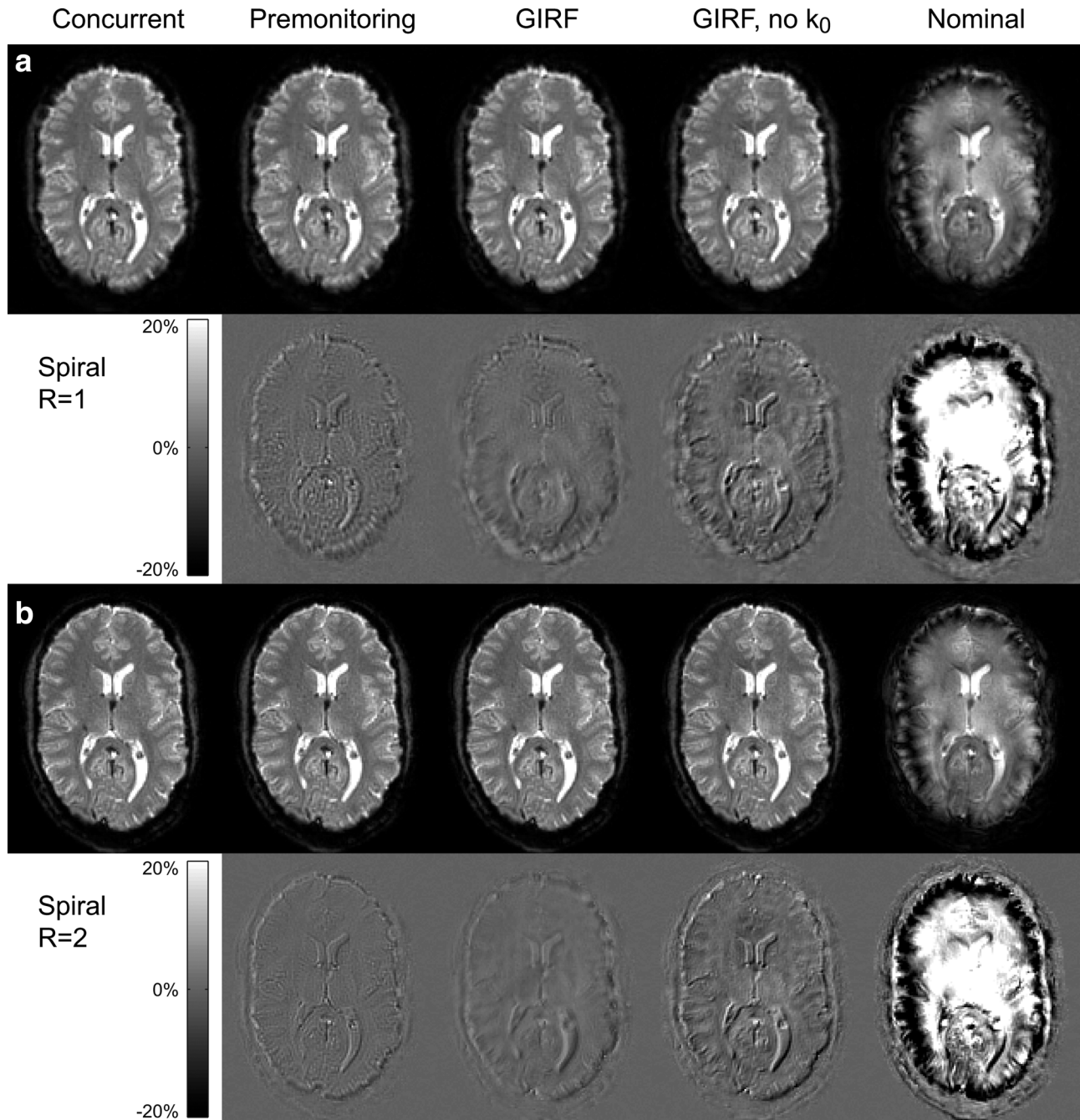


FIG. 9. **a,b:** In vivo images of the acquired spiral trajectories. Reconstructions based on concurrent monitoring, premonitoring, GIRF-predicted trajectories, GIRF-predicted trajectories excluding  $k_0$ , and nominal trajectories are shown, as well as difference images using the reconstruction with concurrently monitored trajectories as a reference. Difference images are scaled to  $\pm 20\%$  of the maximum image value in the concurrently monitored image.

non-Cartesian sampling schemes have received increased attention for the greater flexibility offered in optimizing the sampling pattern to specific objectives, e.g., to render aliasing incoherent for compressed sensing. GIRF-based trajectory prediction could facilitate such efforts both by providing reliable trajectory information for image reconstruction and by aiding the design of gradient time-courses that are physically realizable on a particular system.

Many currently used trajectory correction techniques rely on determining and compensating for gradient

delays. We here compared the suggested GIRF-based reconstruction with a pure gradient delay correction. The latter yielded significantly improved image quality compared with nominal trajectories only in the case of fully sampled EPI sequences. This indicates that, although accurate timing of the gradient system is crucial, a correction based on pure delays is insufficient for many applications. Conversely, all sequences investigated, including standard EPI, benefitted from taking frequency-dependent responses into account by using the full GIRF model.

For EPI sequences, it is common to perform a phase correction that aims to eliminate systematic phase differences between odd and even readout lines, thereby suppressing Nyquist ghosting in the image. This correction approach has largely enabled the present-day widespread use of EPI for fast imaging. Typically, the correction model includes both a linear phase difference, corresponding to a gradient delay, and a constant phase difference. The latter corresponds to a global phase component systematically varying with the readout direction. Interestingly, field monitoring data showed the presence of a 0<sup>th</sup>-order phase component oscillating with the readout gradient. These 0<sup>th</sup>-order oscillations were well predicted by the measured GIRFs and their inclusion in the reconstruction significantly contributed to ghosting reduction in EPI images.

Generally, the GIRF-based method offers the possibility of correcting for cross-term responses of any spatial order, if adequately characterized (24,36). Higher-order field responses have been reported to affect diffusion imaging (20,37), and could speculatively underlie subtle residual ghosting observed in log-scale images of reconstructions based on concurrent monitoring. If known through a higher-order GIRF model, such cross-term effects could be accounted for by higher-order image reconstruction (20).

As any post-acquisition correction approach, GIRF-based reconstruction will deliver satisfactory results only if the acquired signal fundamentally contains the targeted image information. At the k-space level, this requirement translates into sufficient coverage of k-space, sampled in accordance with the Nyquist criterion or, in the case of parallel imaging, a somewhat relaxed density threshold. Excessive field perturbations can cause intrinsic loss of information, leading to ill-conditioned reconstruction.

In cases where insufficient encoding is caused by gradient system imperfection, measured GIRFs could be used as a basis for calculation of pre-emphasis filters to increase gradient fidelity prospectively (38,39). Pre-emphasis filters aim to boost the input signal at frequencies that are attenuated by the native system response. This however comes at the cost of increased power requirements and is limited by hardware constraints. Remaining deviations from ideal gradient dynamics after pre-emphasis can then be addressed by retrospective correction techniques, such as GIRF-based trajectory calculation.

The proposed GIRF-based reconstruction approach is valid to the extent that the gradient system is linear and time-invariant. This is largely true for most significant sources of dynamic field imperfections. Smaller deviations from the model are, however, to be expected from various origins (22,40,41). Minor nonlinear contributions to the system response may for example be caused by gradient amplifier nonlinearities and concomitant fields. The system may also exhibit thermally related time-dependence, and external sources may introduce field fluctuations unrelated to the gradients. Potentially, some of these effects violating the LTI assumption can be dealt with by model extensions or complementary measurements.

In the presented work, field-monitoring data was adjusted for erroneous projections of concomitant field terms onto the spherical harmonic basis set. Building

further upon this approach, the calculated concomitant field terms could be included in a higher-order signal model for image reconstruction (20). Calculation of concomitant field terms can be based on predicted gradient time-courses and the approach could thus be used to augment GIRF-based image reconstruction, as well as monitoring-based reconstruction.

Coil hardware in the magnet bore may host gradient-induced eddy currents that could affect image encoding in a coil-specific manner. It is, therefore, worth noting that the GIRF characterization and the premonitoring performed in this work were obtained with only the body coil present, whereas the concurrent monitoring used field probes attached to the eight-channel receive array used for brain imaging. The good agreement between field evolutions obtained by concurrent monitoring, premonitoring and GIRF-predictions thus indicates that potential eddy-currents in the array setup were minimal. For coils with significant gradient eddy-currents, a set of coil-specific GIRFs could be obtained by field measurements inside the coil, provided that the eddy-current effects are linear and time-invariant.

It has previously been reported that changes in gradient temperature can alter mechanical resonances of the gradient system and their field effects (41). Despite active cooling systems, scans with a heavy gradient duty cycle may heat up the gradient coils together with surrounding supporting materials. The thermal state influences material properties, such as electrical resistance and mechanical elasticity, which in turn can affect the system response. If such changes are sufficiently reproducible, it may be feasible to include thermal parameters in an extended model of the gradient system. Alternatively, GIRF measurements could be acquired under heated conditions and be used to dynamically update the GIRF with the changing state of the scanner.

Field fluctuations that naturally elude the GIRF approach include magnet drifts (22) and dynamic susceptibility effects due to movement of the subject in the scanner (42,43). Slowly varying perturbations can be tracked with navigator techniques (44,45) or snapshot field monitoring (21,46) which thus can yield complementary information to GIRF-based trajectory prediction. If faster field perturbations become critical concurrent field monitoring during scanning is a generic albeit more hardware-demanding alternative.

## ACKNOWLEDGMENTS

The authors thank Marco Jauslin for software contributions. Philips Healthcare is gratefully acknowledged for technical support. This study was supported by The Swiss National Competence Center in Biomedical Imaging (M.H.), the NCCR Neural Plasticity and Repair (L.K.), and an ETH Pioneer Fellowship (C.B.).

## REFERENCES

1. Ahn CB, Kim JH, Cho ZH. High-speed spiral-scan echo planar NMR imaging-I. *IEEE Trans Med Imaging* 1986;5:2-7.
2. Mansfield P. Multi-planar image formation using NMR spin echoes. *J Phys C Solid State Phys* 1977;10:L55.

3. Bruder H, Fischer H, Reinfelder H-E, Schmitt F. Image reconstruction for echo planar imaging with nonequidistant k-space sampling. *Magn Reson Med* 1992;23:311–323.
4. Buonocore MH, Gao L. Ghost artifact reduction for echo planar imaging using image phase correction. *Magn Reson Med* 1997;38:89–100.
5. Van der Zwaag W, Marques JP, Lei H, Just N, Kober T, Gruetter R. Minimization of Nyquist ghosting for echo-planar imaging at ultra-high fields based on a “negative readout gradient” strategy. *J Magn Reson Imaging* 2009;30:1171–1178.
6. Kuhara S, Kassai Y, Ishihara Y, Yui M, Hamamura Y, Sugimoto H. A novel EPI reconstruction technique using multiple RF coil sensitivity maps. In Proceedings of the 8th Annual Meeting of ISMRM, Denver, Colorado, USA; 2000. Abstract 154.
7. Kellman P, McVeigh ER. Ghost artifact cancellation using phased array processing. *Magn Reson Med* 2001;46:335–343.
8. Börner P, Schomberg H, Aldefeld B, Groen J. Improvements in spiral MR imaging. *MAGMA* 1999;9:29–41.
9. Bhavsar PS, Zwart NR, Pipe JG. Fast, variable system delay correction for spiral MRI. *Magn Reson Med* 2014;71:773–782.
10. Spielman DM, Pauly JM. Spiral imaging on a small-bore system at 4.7t. *Magn Reson Med* 1995;34:580–585.
11. Mason GF, Harshbarger T, Hetherington HP, Zhang Y, Pohost GM, Twieg DB. A Method to measure arbitrary k-space trajectories for rapid MR imaging. *Magn Reson Med* 1997;38:492–496.
12. Duyn JH, Yang YH, Frank JA, van der Veen JW. Simple correction method for k-space trajectory deviations in MRI. *J Magn Reson* 1998; 132:150–153.
13. Alley MT, Glover GH, Pelc NJ. Gradient characterization using a Fourier-transform technique. *Magn Reson Med* 1998;39:581–587.
14. Zhang Y, Hetherington HP, Stokely EM, Mason GF, Twieg DB. A novel k-space trajectory measurement technique. *Magn Reson Med* 1998;39:999–1004.
15. De Zanche N, Barmet C, Nordmeyer-Massner JA, Pruessmann KP. NMR probes for measuring magnetic fields and field dynamics in MR systems. *Magn Reson Med* 2008;60:176–186.
16. Barmet C, De Zanche N, Pruessmann KP. Spatiotemporal magnetic field monitoring for MR. *Magn Reson Med* 2008;60:187–197.
17. Barmet C, De Zanche N, Wilm BJ, Pruessmann KP. A transmit/receive system for magnetic field monitoring of in vivo MRI. *Magn Reson Med* 2009;62:269–276.
18. Dietrich BE, Brunner DO, Wilm BJ, Barmet C, Gross S, Kasper L, Haerberlin M, Schmid T, Vannesjo SJ, Pruessmann KP. A field camera for MR sequence monitoring and system analysis. *Magn Reson Med* 2016;75:1831–1840.
19. Barmet C, Wilm BJ, Pavan M, Katsikatsos G, Keupp J, Mens G, Pruessmann KP. Concurrent higher-order field monitoring for routine head MRI: an integrated heteronuclear setup. In Proceedings of the 18th Annual Meeting of ISMRM, Stockholm, Sweden, 2010. Abstract 216.
20. Wilm BJ, Barmet C, Pavan M, Pruessmann KP. Higher order reconstruction for MRI in the presence of spatiotemporal field perturbations. *Magn Reson Med* 2011;65:1690–1701.
21. Vannesjo SJ, Wilm BJ, Duerst Y, Gross S, Brunner DO, Dietrich BE, Schmid T, Barmet C, Pruessmann KP. Retrospective correction of physiological field fluctuations in high-field brain MRI using concurrent field monitoring. *Magn Reson Med* 2015;73: 1833–1843.
22. Kasper L, Bollmann S, Vannesjo SJ, Gross S, Haerberlin M, Dietrich BE, Pruessmann KP. Monitoring, analysis, and correction of magnetic field fluctuations in echo planar imaging time series. *Magn Reson Med* 2015;74:396–409.
23. Addy NO, Wu HH, Nishimura DG. Simple method for MR gradient system characterization and k-space trajectory estimation. *Magn Reson Med* 2012;68:120–129.
24. Vannesjo SJ, Haerberlin M, Kasper L, Pavan M, Wilm BJ, Barmet C, Pruessmann KP. Gradient system characterization by impulse response measurements with a dynamic field camera. *Magn Reson Med* 2013;69:583–593.
25. Graedel NN, Vannesjo SJ, Kasper L, Gross S, Dietrich BE, Barmet C, Pruessmann KP. Image reconstruction using the gradient impulse response for trajectory prediction. In Proceedings of the 21st Annual Meeting of ISMRM, Salt Lake City, Utah, USA; 2013. Abstract 552.
26. Bernstein MA, Zhou XJ, Polzin JA, King KF, Ganin A, Pelc NJ, Glover GH. Concomitant gradient terms in phase contrast MR: analysis and correction. *Magn Reson Med* 1998;39:300–308.
27. Lustig M, Kim S-J, Pauly JM. A fast method for designing time-optimal gradient waveforms for arbitrary k-space trajectories. *IEEE Trans Med Imaging* 2008;27:866–873.
28. Kasper L, Haerberlin M, Dietrich BE, et al. Matched-filter acquisition for BOLD fMRI. *Neuroimage* 2014;100:145–160.
29. Pruessmann KP, Weiger M, Bornert P, Boesiger P. Advances in sensitivity encoding with arbitrary k-space trajectories. *Magn Reson Med* 2001;46:638–651.
30. O’Sullivan JD. A fast sinc function gridding algorithm for Fourier inversion in computer tomography. *IEEE Trans Med Imaging* 1985;4:200–207.
31. Jackson JI, Meyer CH, Nishimura DG, Macovski A. Selection of a convolution function for Fourier inversion using gridding [computerized tomography application]. *IEEE Trans Med Imaging* 1991;10:473–478.
32. Beatty PJ, Nishimura DG, Pauly JM. Rapid gridding reconstruction with a minimal oversampling ratio. *IEEE Trans Med Imaging* 2005;24: 799–808.
33. Man L-C, Pauly JM, Macovski A. Multifrequency interpolation for fast off-resonance correction. *Magn Reson Med* 1997;37:785–792.
34. Sutton BP, Noll DC, Fessler JA. Fast, iterative image reconstruction for MRI in the presence of field inhomogeneities. *IEEE Trans Med Imaging* 2003;22:178–188.
35. Barmet C, Tsao J, Pruessmann KP. Sensitivity encoding and B0 inhomogeneity - a simultaneous reconstruction approach. In Proceedings of the 13th Annual Meeting of ISMRM, Miami, Florida, USA, 2005. Abstract 682.
36. Vannesjo SJ, Dietrich BE, Pavan M, Brunner DO, Wilm BJ, Barmet C, Pruessmann KP. Field camera measurements of gradient and shim impulse responses using frequency sweeps. *Magn Reson Med* 2014; 72:570–583.
37. Xu D, Maier JK, King KF, Collick BD, Wu G, Peters RD, Hinks RS. Prospective and retrospective high order eddy current mitigation for diffusion weighted echo planar imaging. *Magn Reson Med* 2013;70: 1293–1305.
38. Vannesjo SJ, Dietrich BE, Barmet C, Wilm BJ, Brunner DO, Pruessmann KP. Measurement and pre-emphasis of shim responses using frequency sweeps. In Proceedings of the 20th Annual Meeting of ISMRM, Melbourne, Australia, 2012. Abstract 142.
39. Goora FG, Colpitts BG, Balcom BJ. Arbitrary magnetic field gradient waveform correction using an impulse response based pre-equalization technique. *J Magn Reson* 2014;238:70–76.
40. Brodsky EK, Samsonov AA, Block WF. Characterizing and correcting gradient errors in non-cartesian imaging: are gradient errors linear time-invariant (LTI)? *Magn Reson Med* 2009;62:1466–1476.
41. Busch J, Vannesjo SJ, Barmet C, Pruessmann KP, Kozerke S. Analysis of temperature dependence of background phase errors in phase-contrast cardiovascular magnetic resonance. *J Cardiovasc Magn Reson* 2014;16:97.
42. Raj D, Paley DP, Anderson AW, Kennan RP, Gore JC. A model for susceptibility artefacts from respiration in functional echo-planar magnetic resonance imaging. *Phys Med Biol* 2000;45:3809.
43. Van de Moortele P, Pfeuffer J, Glover GH, Ugurbil K, Hu X. Respiration-induced B0 fluctuations and their spatial distribution in the human brain at 7 Tesla. *Magn Reson Med* 2002;47:888–895.
44. Hu X, Kim S-G. Reduction of signal fluctuation in functional MRI using navigator echoes. *Magn Reson Med* 1994;31:495–503.
45. Versluis MJ, Sutton BP, de Bruin PW, Börner P, Webb AG, van Osch MJ. Retrospective image correction in the presence of nonlinear temporal magnetic field changes using multichannel navigator echoes. *Magn Reson Med* 2012;68:1836–1845.
46. Duerst Y, Wilm BJ, Dietrich BE, Vannesjo SJ, Barmet C, Schmid T, Brunner DO, Pruessmann KP. Real-time feedback for spatiotemporal field stabilization in MR systems. *Magn Reson Med* 2015;73:884–893.

## SUPPORTING INFORMATION

Additional Supporting Information may be found in the online version of this article.

**Table S1.** Root-mean-square magnitude differences between the GIRFs acquired recently and 3 years prior, evaluated within different frequency bands. The values are given in percent of the normalized DC self-term response.